



**CHALMERS**  
UNIVERSITY OF TECHNOLOGY

## **Plasma Cleaning of Cationic Surfactants from Pd Nanoparticle Surfaces: Implications for Hydrogen Sorption**

Downloaded from: <https://research.chalmers.se>, 2024-03-20 10:54 UTC

Citation for the original published paper (version of record):

Darmadi, I., Piella Bagaria, J., Stolas, A. et al (2023). Plasma Cleaning of Cationic Surfactants from Pd Nanoparticle Surfaces: Implications for Hydrogen Sorption. ACS Applied Nano Materials, 6(10): 8168-8177.  
<http://dx.doi.org/10.1021/acsanm.3c00141>

N.B. When citing this work, cite the original published paper.

# Plasma Cleaning of Cationic Surfactants from Pd Nanoparticle Surfaces: Implications for Hydrogen Sorption

Iwan Darmadi,\* Jordi Piella, Alicja Stolaś, Carl Andersson, Christopher Tiburski, Kasper Moth-Poulsen, and Christoph Langhammer\*



Cite This: *ACS Appl. Nano Mater.* 2023, 6, 8168–8177



Read Online

ACCESS |

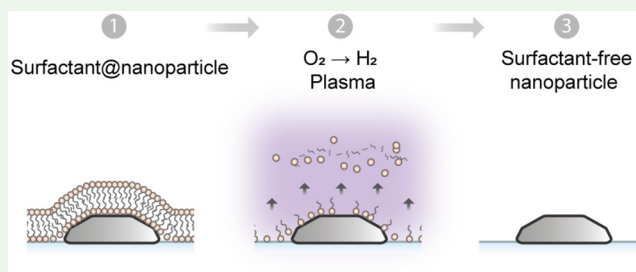
Metrics & More

Article Recommendations

Supporting Information

**ABSTRACT:** Cationic surfactants are widely used in the colloidal synthesis of noble metal nanoparticles in general, and of Pd nanoparticles in particular, to stabilize them toward aggregate formation in solution and to promote shape-specific particle growth. Despite the benefits at the synthesis stage, these surfactants can be problematic once the nanoparticles are to be applied as they may both geometrically block and electronically alter surface sites that are important for surface chemical reactions. This is particularly relevant in applications like bio- and chemosensors where analyte-nanoparticle surface interactions constitute the actual sensing event. Here,  $H_2$  sensors based on Pd and its alloys are no exception since the dissociation of  $H_2$  on the particle surface is the first step toward hydride formation and thus hydrogen detection, and it has been demonstrated that the presence of surfactant molecules detrimentally affects the hydrogen sorption rate. Here, we therefore develop a scheme to remove cationic surfactants from Pd nanoparticle surfaces by means of subsequent  $O_2$  and  $H_2$  plasma treatment, whose effectiveness we verify by X-ray photoelectron spectroscopy. Furthermore, we find that the plasma treatment both alters the surface structure of the Pd nanoparticles at the atomic level and leads to surface contamination by so-called  $H_2$  plasma swift chemical sputtering of Al, Si and F species present in the plasma chamber, which in combination significantly reduce hydrogen sorption rates and increase apparent activation energies, as revealed by plasmonic hydrogen sorption kinetic measurements. Finally, we show that both these effects can be reversed by mild thermal annealing and that after the complete plasma cleaning–thermal annealing sequence hydrogen sorption rates essentially identical to the ones of neat Pd particles never exposed to cationic surfactants can be achieved. This advertises tailored plasma cleaning and mild heat treatments as an effective recipe for the removal of surfactant molecules from nanoparticle surfaces.

**KEYWORDS:** palladium, hydrogen, hydride, cationic surfactant, nanoparticle,  $H_2$  plasma,  $O_2$  plasma, plasma treatment



## INTRODUCTION

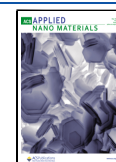
Pd films and nanoparticles, and their derivatives in terms of alloys, find wide application in processes and technologies where the interaction of molecules with their surfaces is a key step, such as in heterogeneous catalysis,<sup>1–3</sup> gas storage,<sup>4,5</sup> gas separation membranes,<sup>6,7</sup> and gas sensors.<sup>8–12</sup> In this context, the interaction of Pd surfaces with hydrogen gas is an interesting subcategory,<sup>7,8,13,14</sup> where many applications exploit the exceptional ability of Pd to efficiently dissociate molecular hydrogen ( $H_2$ ) at ambient conditions and absorb H into its lattice in interstitial sites, eventually forming a hydride.<sup>15</sup> In many of these applications, the kinetics of  $H_2$  dissociation and/or absorption and desorption into/from the interstitial sites in the Pd lattice is a crucial aspect of the targeted performance because it determines, for instance, kinetics of a catalytic reaction,<sup>16,17</sup> response times of hydrogen sensors,<sup>9,18–20</sup> or the loading time of a hydrogen storage medium.<sup>21</sup> It is therefore clear that the state of the surface plays a critical role when defining the barriers of the rate

limiting step, which on a clean Pd surface for hydrogen absorption is the step from the surface to the first subsurface site<sup>22</sup> and associative desorption of  $H_2$  from the surface for the reverse process.<sup>23</sup> However, it has also been shown that surface contaminants such as carbon monoxide (CO)<sup>24–26</sup> and sulfuric or sulfidic compounds (e.g.,  $SO_2$  and  $H_2S$ ),<sup>27–29</sup> as well as surfactant molecules used for colloidal synthesis of Pd nanocrystals<sup>30,31</sup> distinctly affect the rate of hydrogen sorption and the corresponding energetics.<sup>32,33</sup> At the same time, surface contamination is unavoidable upon exposure to ambient conditions or in colloidal Pd nanoparticle synthesis due to the multiple key roles of surfactants/capping agents,

**Received:** January 10, 2023

**Accepted:** April 24, 2023

**Published:** May 4, 2023



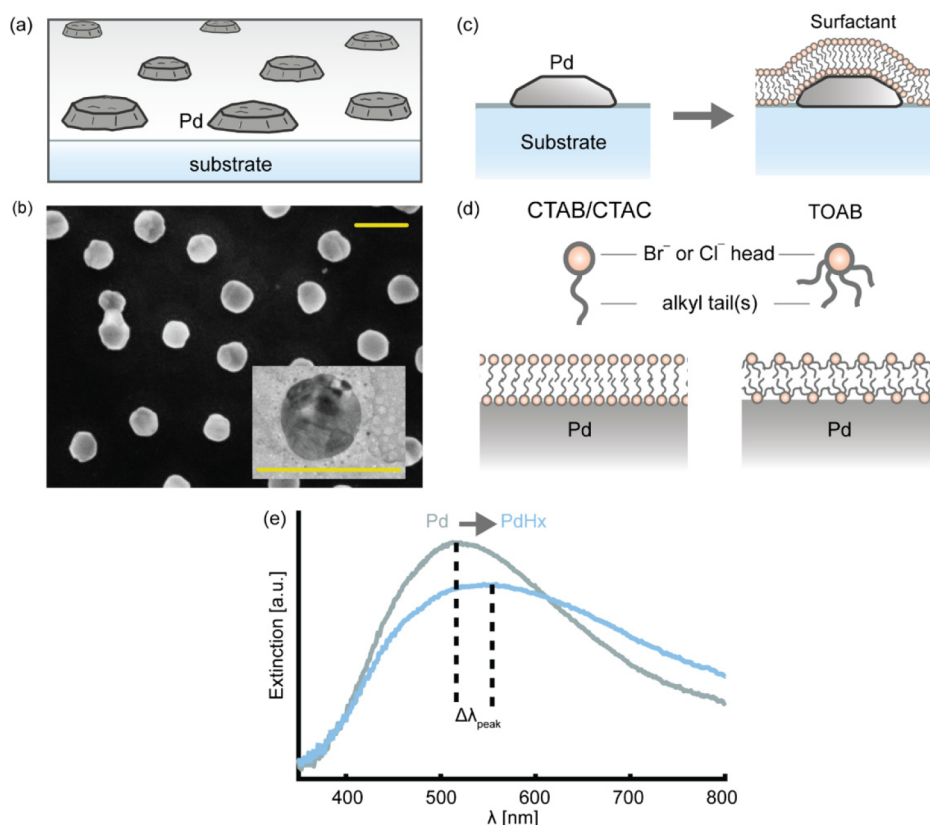


**Figure 1.** (a) Artist rendition of a quasi random Pd nanoparticle array nanofabricated onto flat support, such as a Si or fused silica wafer used in this work. (b) SEM and (inset) TEM image of the Pd nanoparticles used for this study (both scale bars are 200 nm). (c) Schematic depiction of the cationic surfactant molecule coating on a Pd nanoparticle surface (not to scale). (d) Illustrations of CTAB, CTAC, and TOAB molecular structures and their respective bilayer formation on a Pd surface (not to scale). (e) Optical extinction spectrum of an array of Pd nanoparticles as shown in b exhibiting a distinct localized surface plasmon resonance (LSPR) peak at  $\sim 520$  nm plotted together with an extinction spectrum measured for the same array but with the Pd in its hydride state, PdH<sub>x</sub>. The spectral position of the LSPR peak ( $\Delta\lambda_{\text{peak}}$ ) scales linearly with the H/Pd ratio.<sup>49</sup>

such as solubilizing the initial reagents, directing shape-selected particle growth, and preventing nanoparticle aggregation in suspension.<sup>34</sup>

Among these capping agents, surfactants of the cationic-type that are based on quaternary ammonium salts, for example, CTAB (cetyltrimethylammonium bromide), CTAC (cetyltrimethylammonium chloride), and TOAB (tetraoctylammonium bromide), are widely used since they adsorb on the nanoparticle surface providing both steric and electrostatic stabilization against aggregation.<sup>35–38</sup> At the same time, their selective adsorption onto specific crystalline facets constitutes the basis for the shape-controlled synthesis of most metal nanoparticles in general and Pd in particular.<sup>39–41</sup> However, in this adsorption process, the halide ions ( $\text{Br}^-$  or  $\text{Cl}^-$ ) bind strongly to the Pd surface<sup>39,42</sup> and thereby effectively block a significant fraction of surface sites, such as the  $\text{H}_2$  dissociation (recombination) sites of particular interest here, from access for other species, which leads to a significant decrease in hydrogen sorption rate.<sup>32</sup> Furthermore, the metal-halide bond locally alters the electronic landscape of the surface and thereby the relevant activation barriers during the hydrogen sorption process.<sup>32</sup>

To this end, numerous attempts have been made to remove cationic-type surfactant molecules from metallic nanoparticle surfaces using electrochemistry,<sup>43,44</sup> chemical<sup>45</sup> or heat-treatment,<sup>45</sup> and UV-ozone cleaning.<sup>3,46</sup> While electrochemical cleaning has been shown to be efficient, its applicability is limited. Heat treatment potentially deforms and aggregates the

nanoparticles. In the UV-ozone cleaning process, ionized species of oxygen in combination with UV-light are used to remove the contaminants via chemical reactions between ions and contamination that form readily desorbing volatile compounds.<sup>47</sup> Despite its effectiveness, UV-ozone cleaning (as well as heat-treatment and chemical cleaning) usually requires long processing times. For example, UV-ozone and heat treatments that remove cationic-type surfactants from Pd surfaces have been reported to take several hours<sup>33,45</sup> and even more time-consuming chemical cleaning procedures using, e.g., *tert*-butylamine (TBA) solution to remove  $\text{Br}^-$  take up to 3 days.<sup>46</sup> In addition, heat and UV-ozone treatments tend to oxidize Pd. Due to those limitations, a more efficient and benign approach to remove cationic-type surfactant molecules from metal nanoparticle surfaces in general and from Pd surfaces in particular is important to be developed.

In this work, we therefore develop and investigate in detail the removal of the three cationic surfactants CTAB, CTAC and TOAB from nanofabricated Pd nanoparticle surfaces by means of  $\text{H}_2$  plasma and  $\text{O}_2$  plasma, and its impact on the hydrogen sorption properties of these particles, as well as on their surface structure. For this purpose, we use high-resolution X-ray photoelectron spectroscopy (XPS) and transmission electron microscopy (TEM) in combination with localized surface plasmon resonance (LSPR) based hydrogen sorption rate measurements.<sup>9</sup> Specifically, we execute our experiments on the basis of initially surfactant-free nanoparticles immobi-

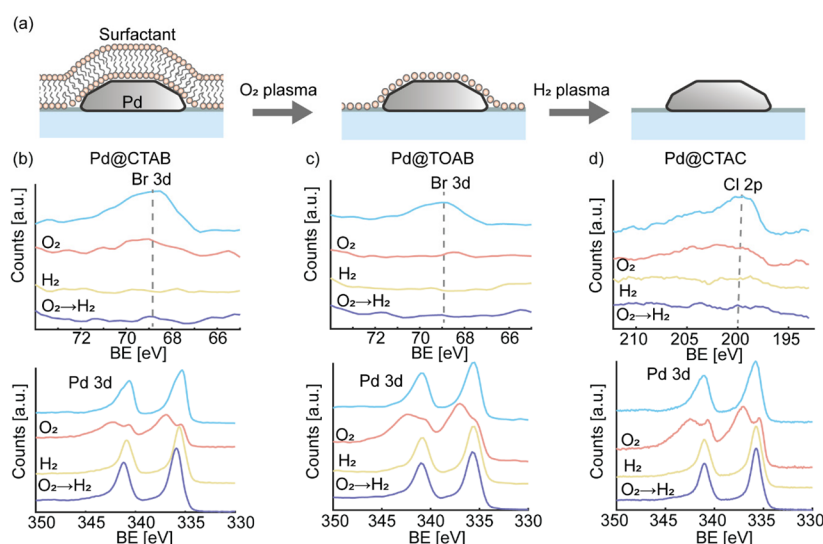


**Figure 2.** (a) Schematic of surfactant removal using sequential O<sub>2</sub> plasma and H<sub>2</sub> plasma treatment. O<sub>2</sub> plasma removes the surfactants' alkyl tail and likely the non-Pd-binding cations, while H<sub>2</sub> plasma removes the halide cations from the Pd surface. High-resolution Pd 3d and Br 3d/Cl 2p XPS spectra of (b) Pd@CTAB, (c) Pd@TOAB, and (d) Pd@CTAC with the respective plasma treatments: (i) O<sub>2</sub> plasma, (ii) H<sub>2</sub> plasma, and (iii) sequential O<sub>2</sub> plasma → H<sub>2</sub> plasma.

lized on a surface by nanofabrication (rather than actually using colloidal Pd nanoparticles synthesized in solution) that we subsequently expose to different capping agents, following a scheme we have introduced earlier.<sup>48</sup> This approach enables the tracking of the impact of the cleaning process on the nanoparticle structure and function in an efficient way, since a control experiment from the pristine, surfactant-free, and uncleaned sample is always readily available as the first step of a series of experiments.

## RESULTS AND DISCUSSION

The quasi-random arrays of Pd nanoparticles (Figure 1a) used for this study were nanofabricated onto flat fused silica (for optical hydrogen sorption measurements) or oxidized Si wafer (for XPS) substrates using the hole-mask colloidal lithography method described in detail in our previous work<sup>20,24,48</sup> and in brief in the Methods section. After fabrication, we annealed the nanoparticle arrays at 500 °C for 24 h in 4% H<sub>2</sub> in Ar carrier gas to induce recrystallization into polycrystalline structures with few grains and low index surface facets<sup>50,51</sup> (Figure 1b). To subsequently self-assemble a bilayer of surfactants onto the particles,<sup>32,38</sup> we drop-cast CTAB, TOAB, or CTAC water solutions (10 mM), respectively, onto the sample and left it incubate for 24 h (Figure 1c). Excess solution was subsequently rinsed-off with Milli-Q water, followed by drying in a N<sub>2</sub> stream. Here, we note that CTAB and CTAC have similar molecular structures with one long alkyl tail but are distinct in their counterion, i.e., Br<sup>−</sup> in CTAB and Cl<sup>−</sup> in CTAC, with which they bind to the Pd surface<sup>35,36,39,52</sup> (Figure 1d). At the same time, CTAB and TOAB feature cationic quaternary ammonium but the former has one long alkyl chain, whereas the latter has four shorter tails. As a consequence of the different steric hindrance exhibited by these tails, CTAB and CTAC form a denser layer compared to TOAB, as illustrated schematically in Figure 1d.<sup>53–55</sup> Finally, to investigate both the impact of the presence of the surfactants and subsequently of the plasma cleaning procedures on the state of surface activity of the Pd nanoparticles, we monitored the hydrogen sorption rate using localized surface

plasmon resonance (LSPR) based sensing, according to the principle illustrated in Figure 1e, which tracks the LSPR peak position while the nanoparticle (de)absorbs hydrogen.<sup>9</sup> Since the LSPR peak position shift ( $\Delta\lambda_{\text{peak}}$ ) scales linearly with the H/Pd ratio,<sup>49</sup> its temporal evolution represents the hydrogen sorption rate, which is dictated by the rate-limiting H-diffusion step from the surface to the first subsurface layer for absorption.<sup>22,56</sup> Hence, it is expected to be directly affected by the presence of surface contamination<sup>20,25,32,57</sup> and changing surface structure,<sup>23,58,59</sup> and thus to be well-suited to serve as a model reaction for investigating the impact of plasma cleaning on the surface reactivity of Pd nanoparticles.

To start this investigation, we prepared five samples, wherein one was kept as-is after nanofabrication and annealing to serve as negative control (neat Pd). The remaining three samples were coated with a bilayer of CTAB (Pd@CTAB), CTAC (Pd@CTAC), or TOAB (Pd@TOAB), respectively, using the procedure outlined above. For each surfactant type, the four samples subsequently underwent different treatment: (i) the first sample was kept as-coated, while the remaining three were treated with (ii) O<sub>2</sub> plasma, (iii) H<sub>2</sub> plasma, or (iv) O<sub>2</sub> plasma and H<sub>2</sub> plasma in sequence (see the schematic in Figure 2a and the Methods section for plasma dosage details).

Focusing first on Pd@CTAB, XPS analysis reveals a distinct Br 3d peak (BE ≈ 68.8 eV) for as-deposited Pd@CTAB, which decreases significantly after both O<sub>2</sub> and H<sub>2</sub> plasma treatments (Figure 2b). Closer inspection shows that H<sub>2</sub> plasma appears to have completely removed the Br<sup>−</sup> (reduction from 6.3 at. % to 0.0 at. %) within the elemental quantification resolution limit of 0.4–1.0 at. % of the used XPS system, whereas after the O<sub>2</sub> plasma treatment some trace of Br<sup>−</sup> is still measurable (reduced from 6.3 at. % to 1.9 at. %) (Figure 2a and Table S1 for more detailed quantitative analysis). Most likely, the O<sub>2</sub> plasma removes the Br<sup>−</sup> of the outer layer of the bilayer (the one that does not bind to Pd) as illustrated in Figure 2a. As a second key point, analyzing the Pd 3d peaks for these three samples reveals the appearance of distinct “shoulders” in the spectrum after the O<sub>2</sub> plasma, which indicates significant surface oxidation of the Pd particles. Notably, these shoulders



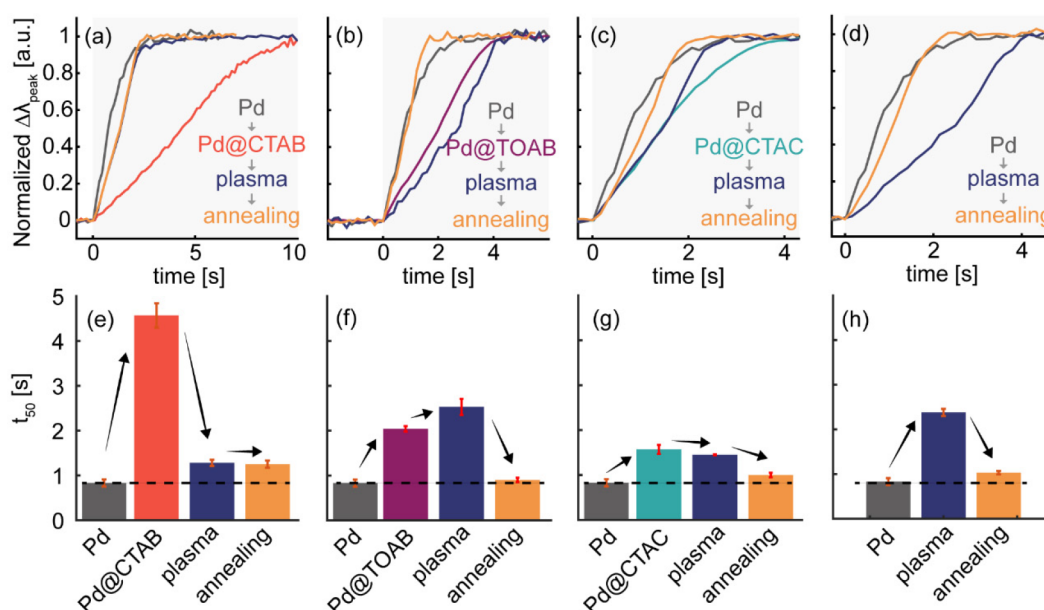


**Figure 3.** Temporal response of (a) Pd@CTAB, (b) Pd@TOAB, (c) Pd@CTAC, and (d) neat Pd to a stepwise 0 → 320 mbar  $H_2$  pressure change at 30 °C before and after plasma-annealing treatments. The pressure change was executed at  $t = 0$  s. The response was measured after (i)  $O_2$  plasma →  $H_2$  plasma (blue) and (ii)  $O_2$  plasma →  $H_2$  plasma → 250 °C annealing (yellow).  $t_{50}$ , that is, the time to reach 50% of the total normalized response for (e) Pd@CTAB, (f) Pd@TOAB, (g) Pd@CTAC, and (h) neat Pd, respectively. The error bars are the standard deviation obtained from three measurements. The arrows highlight the trend after each treatment step.

are absent both for the as-deposited Pd@CTAB sample and after  $H_2$  plasma. This is expected due to the oxidizing and reducing nature of  $O_2$  and  $H_2$  plasma treatments, respectively. Hence, in principle, these findings would advertise  $H_2$  plasma as the superior solution due to both its superior halogen species removing performance and benign properties with respect to inducing surface oxidation, that we also confirmed for Pd@TOAB (Figure 2c) and Pd@CTAC (Figure 2d; see the quantitative analysis in Table S1). Unfortunately, however, it has also been shown that  $H_2$  plasma is inefficient for the removal of carbonaceous species, which in our present case translates to the alkyl tail(s) of the surfactant molecules.<sup>60</sup> Therefore,  $O_2$  plasma in combination with  $H_2$  plasma is necessary to remove the surfactant molecule completely. Furthermore, as the corresponding XPS analysis reveals for all three surfactants, subsequent  $O_2$  plasma and  $H_2$  plasma treatment ( $O_2 \rightarrow H_2$ ) not only removes the surfactants but also leaves the Pd surface in its reduced metallic state (Figure 2b–d).

Having established this  $O_2 \rightarrow H_2$  plasma cleaning scheme (below simply referred to as “plasma treatment”), it is now interesting to investigate its impact on the  $H_2$  absorption rate for the Pd@CTAB, Pd@TOAB and Pd@CTAC systems, as well as an uncoated neat Pd control (Figure 3a–d). As observed previously,<sup>32</sup> formation of the surfactant bilayer on the Pd significantly decelerates the  $H_2$  absorption rate, with CTAB having the strongest deceleration effect, followed by TOAB and CTAC. As we have shown, this is the consequence of both (i) the surfactant packing density that hinders the  $H_2$  diffusion to the Pd surface and (ii) the  $Br^-$  (or  $Cl^-$ ) – Pd bond, which decreases the number of  $H_2$  dissociation sites on the Pd surface.<sup>32</sup> Accordingly, although both have identical  $Br^-$  counterions, TOAB is less densely packed on the Pd surface than CTAB due to its bulkier molecular structure, which explains TOAB’s more moderate deceleration effect compared to CTAB. On the other hand, although CTAC has a similar

packing density as CTAB in the bilayer, the deceleration effect is weaker because the  $Cl$ –Pd interaction is weaker than that of  $Br$ –Pd.<sup>39,42</sup>

Having established the impact of the three different surfactants on the hydrogen absorption rate, we now assess the effect of subsequent plasma treatment. Evidently, plasma treatment of Pd@CTAB recovers its  $H_2$  absorption rate, defined as  $t_{50}$  at which 50% of the signal change  $\Delta\lambda_{peak}$  has occurred, from 4.6 to 1.3 s (Figure 3a, e). This is, however, still significantly slower than the absorption rate of the bare Pd measured on the same sample prior to applying the CTAB, i.e., 0.8 s (Figure 3e). Executing the same sequence of experiments on the Pd@TOAB (Figure 3b, f) and Pd@CTAC (Figure 3c, g) systems yields a very similar conclusion. Despite the complete removal of the surfactants by the plasma treatment confirmed by XPS, the original hydrogen absorption rate measured prior to surfactant deposition on each sample is not completely recovered. In fact, and even more intriguingly, plasma treatment further decelerates the hydrogen absorption rate of the Pd@TOAB system. Finally, we also note that we consistently make the same observations for the reversed process, i.e., hydrogen desorption (Figure S1).

To shed light on this surprising effect, we executed the same experimental sequence on a neat Pd sample that had never been exposed to any surfactant and found that also in this case plasma treatment significantly slows down the hydrogen absorption rate from  $t_{50} = 0.8$  s to  $t_{50} = 2.4$  s (Figure 3d, h). Hence, this observation indicates that plasma treatment instigates an additional effect on the system beyond surfactant removal. Interestingly, it is therefore only after 12 h of annealing at 250 °C in 4 vol %  $H_2$  in Ar carrier that the absorption rates are almost completely recovered. In fact, the absorption rate recovers almost completely to the  $t_{50} = 0.8$  s value of the pristine Pd, i.e., Pd@CTAB recovers to  $t_{50} = 1.3$  s, Pd@TOAB recovers to  $t_{50} = 0.9$  s, and Pd@CTAC recovers to  $t_{50} = 1.0$  s (Figure 3 and Figure S1 for desorption).

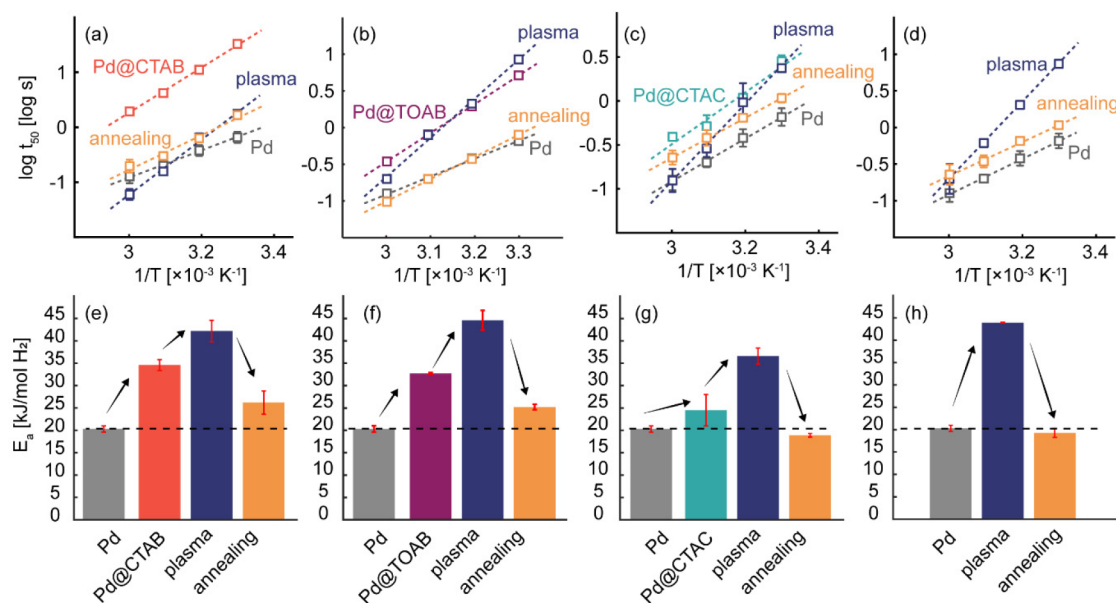


**Figure 4.** Hydrogen absorption Arrhenius plots for (a) Pd@CTAB, (b) Pd@TOAB, (c) Pd@CTAC, and (d) the neat Pd control, respectively, obtained by measuring the absorption kinetics at 30 °C, 40 °C, 50 °C, and 60 °C. The error bar in each data point denotes the standard deviation from three measurements. The absence of an error bar indicates that it is smaller than the symbol size. Apparent hydrogen absorption activation energy,  $E_a$  for (e) Pd@CTAB, (f) Pd@TOAB, (g) Pd@CTAC, and (h) the neat Pd control, calculated from the slope of the Arrhenius plots in a–d, respectively. The error bar denotes the linear-regression uncertainty of the Arrhenius plot. The arrows are guides to the eye that highlight the trend after each treatment step.

The distinct impact of the plasma treatment on the  $\text{H}_2$  absorption kinetics is further manifested in the corresponding apparent activation energy,  $E_a$ , derived by Arrhenius analysis (Figure 4). Clearly, after plasma treatment,  $E_a$  increases by about a factor of 2 from 20.3 kJ/mol  $\text{H}_2$  to 43.9 kJ/mol  $\text{H}_2$  for neat Pd, to 42.2 kJ/mol  $\text{H}_2$  for Pd@CTAB, to 44.6 kJ/mol  $\text{H}_2$  for Pd@TOAB and to 36.6 kJ/mol  $\text{H}_2$  for Pd@CTAC. Similar trends we also again observed for the reverse process of hydrogen desorption (Figure S2) and the annealing step recovers  $E_a$  to close to the initial value, i.e., to 19.3 kJ/mol  $\text{H}_2$  for neat Pd, to 26.0 kJ/mol  $\text{H}_2$  for Pd@CTAB, to 25.2 kJ/mol  $\text{H}_2$  for Pd@TOAB, and to 18.9 kJ/mol  $\text{H}_2$  for Pd@CTAC (Figure 4 and Figure S2 for desorption).

To investigate the reason causing this effect, we performed an XPS survey scan of a plasma treated Pd nanoparticle sample (never exposed to surfactants). This scan (Figure S3) reveals the presence of two unexpected species on the surface: Al and F (Figure 5). Both Al and F can be traced back to the plasma chamber (anode) since the chamber itself is comprised of aluminum and since the same chamber also is used for reactive ion etching using  $\text{CF}_4$ . Since these species are not observed in the XPS scans of samples that we placed on a clean 4 in. Si wafer shield (Figure 5a) it is clear that the origin of Al and F on the samples indeed is the plasma chamber. Mechanistically, it can be understood as so-called swift chemical sputtering of these species by the  $\text{H}_2$  plasma.<sup>61</sup> Finally, we note that also the use of an Si wafer shield will not completely avoid surface contamination during  $\text{H}_2$  plasma treatment since an XPS control measurement on an Au film sample that rested on the Si wafer shield during  $\text{H}_2$  plasma treatment indeed shows Si contamination (Figure S4). As the main conclusion from this analysis, we note that, in principle, all measured contaminants might detrimentally influence  $\text{H}_2$  sorption kinetics. However, among the found three species it is likely that F<sup>−</sup> contamination is the most relevant one due to its strong

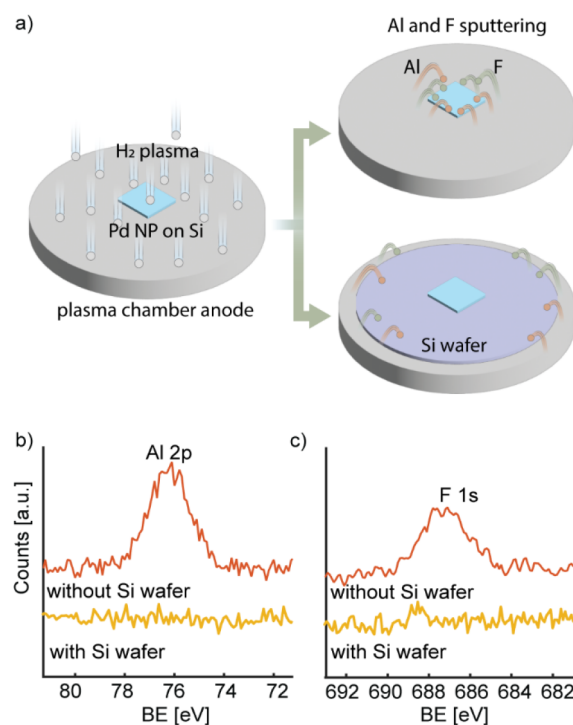


**Figure 5.** (a) Schematic depiction of the mechanism behind the secondary  $\text{H}_2$  plasma sputtering of Al and F contamination onto the Pd nanoparticle sample from the aluminum plasma chamber (anode) and how it can be prevented by using a clean Si wafer as sample support (“shield”) during plasma treatment. We note that the F contamination has its origin from the plasma chamber that is also used for  $\text{CF}_4$  reactive ion etching. High-resolution XPS spectra of the Al 2p (b) and F 1s (c) energy range revealing a distinct Al and F peak, respectively, and their absence when a Si wafer support was used during the plasma treatment.

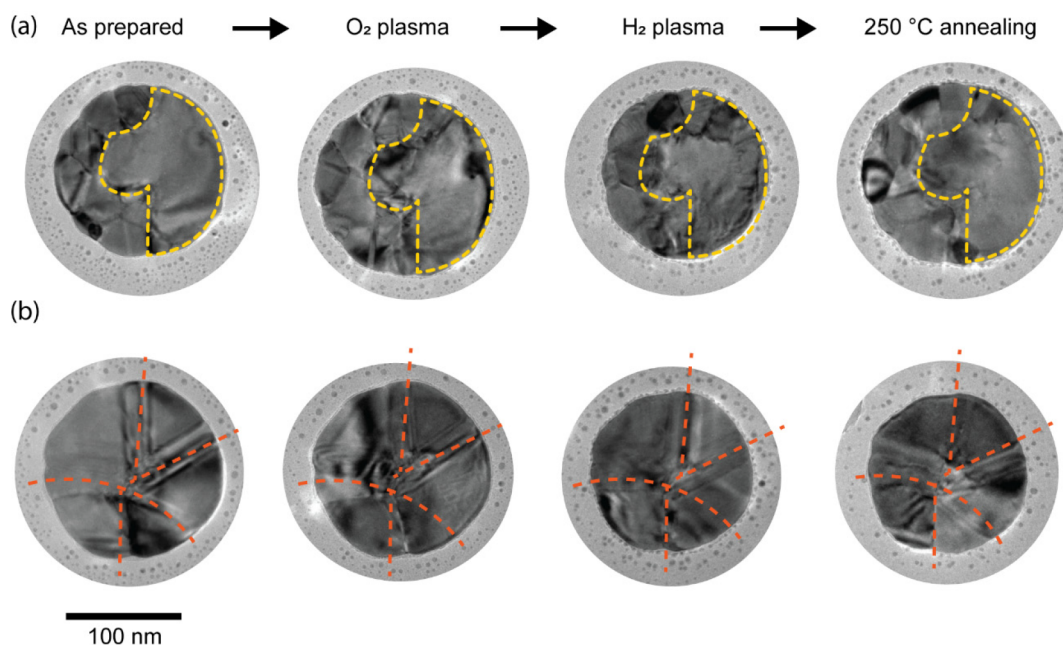


**Figure 6.** Transmission electron microscope images of two representative Pd nanoparticles taken (i) as prepared, (ii) after O<sub>2</sub> plasma, (iii) after H<sub>2</sub> plasma, and (iv) after 250 °C annealing. (a) Image sequence for nanoparticle #1 where the yellow dashed-line highlighted area indicates a region with significant surface roughness changes. (b) Image sequence for nanoparticle #2 where the red dashed lines signify grain boundaries. Note that the nanoparticle grain boundaries, shape, and size are virtually unchanged after the plasma and annealing treatments.

affinity to Pd, which is similar to other halides, such as Br<sup>−</sup> and Cl<sup>−</sup>, which has been demonstrated to significantly slow down hydrogen sorption.<sup>39</sup>

To also investigate potential structural reasons of the decelerated hydrogen sorption kinetics after plasma treatment, we took a series of intermittent transmission electron microscope (TEM) images along the entire plasma treatment sequence (Figure 6). The obtained images from two Pd particles reveal that particle size, shape and grain structure remain essentially unchanged, while the dark/bright regions slightly change (Figure 6a, b and Figure S5 for images of additional particles). Although TEM imaging is not a surface characterization technique, the observed evolution of the image contrast upon plasma treatment provides some insight into nanoparticle surface restructuring. Specifically, the darker regions might stem from high diffraction angles which can be inferred from induced strain or defects on the surface, as reported, for example, for lattice dislocations and stacking faults.<sup>62,63</sup> This effect is particularly apparent after the H<sub>2</sub> plasma treatment step (Figure 6a, dashed-line highlighted region) and in line with earlier reports of plasma treatments structurally altering Pd surfaces at the atomic level.<sup>64,65</sup> Furthermore, atomic force microscopy (AFM) topographical scans of representative nanoparticles corroborate the surface structuring as a significant increase of surface roughness from  $0.1 \pm 0.0$  nm on a pristine Pd nanoparticle to  $0.8 \pm 0.0$  nm after H<sub>2</sub> plasma treatment (Figure 7. For additional sampling details refer to Figure S6 and Table S3). This increasing surface roughness likely induces defects and thus local lattice strain. This is a relevant observation because it is well-known that  $E_a$  of hydrogen sorption in Pd is correlated with surface structure.<sup>23,58,66,67</sup> Finally, the last TEM images in the sequence taken after the 12 h annealing at 250 °C in 4 vol % H<sub>2</sub> in Ar carrier gas reveal that a smooth particle surface reminiscent of the initial state can be recovered, while again

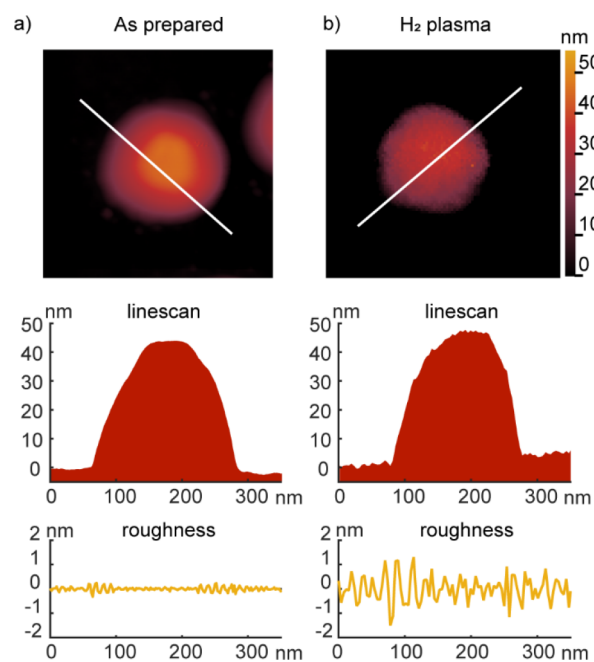


**Figure 7.** Atomic force microscopy (AFM) topography linescan and roughness analysis of representative Pd nanoparticles (a) as prepared and (b) after H<sub>2</sub> plasma treatment.

leaving particle size, shape and grain structure essentially unchanged (Figure 6a, b). It is worth noting that although the annealing induces a smoother surface, a precise recovery to the very initial state was not accomplished (compare the first and fourth columns of Figure 6).

Similarly, investigating the evolution of the Al and F contamination after 6 and 12 h of annealing using XPS reveals a distinct reduction of the F contamination over time from 4.6 to 0.5 at. % while leaving the Al concentration essentially



constant (Figure 8 and Table S2). Here we, however, note that Al is distributed homogeneously over the entire sample surface

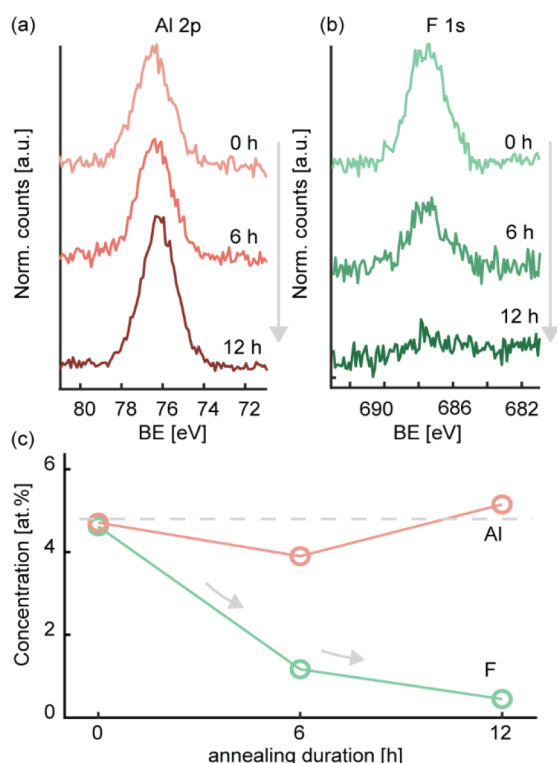


**Figure 8.** Time-evolution of high-resolution XPS spectra taken in the energy range of the (a) Al 2p and (b) F 1s peak. The spectra were taken directly after the sputtering sequence ( $t = 0$  h) and after the Pd nanoparticles had been annealed for 6 and 12 h at 250 °C in 4%  $H_2$  in Ar carrier gas. (c) Al and F surface concentration in at. % as determined from the XPS spectra in panels a and b plotted as a function of annealing time.

during the plasma cleaning. This means that it is also present in between the Pd nanoparticles on the substrate, an area that corresponds to approximately 90% of the sample surface due to the approximately 10% coverage of the Pd nanoparticles. Second, we note that Pd and Al form a solid solution in the relevant Al concentration regime,<sup>68</sup> which means that the Al contamination on the Pd is dissolved into the particles during the annealing. Since Al is present only in trace amounts from the beginning, its concentration in the solid solution in the Pd particles is so low that it very likely does not sizably affect the hydrogen sorption kinetics—in line with the observed almost perfect recovery. Consequently, the measured remaining Al XPS signal stems to the largest extent from the sample areas *between* the Pd nanoparticles where Al remains and likely also coalesces/sinters into tiny particles during the annealing, which may explain the slight variation in XPS signal.

## CONCLUSIONS

We have developed an efficient cationic surfactant molecule removal strategy and illustrated it on the example of Pd nanoparticles. It comprises subsequent  $O_2$  plasma and  $H_2$  plasma treatments to remove the alkyl tail(s) and halide headgroups, respectively, as confirmed by high resolution XPS, followed by a gentle thermal annealing step to restore the surface state of the particles to preplasma conditions and to mitigate surface contamination from the plasma chamber

induced by the  $H_2$  plasma cleaning step. We have demonstrated the validity of this approach by investigating the hydrogen sorption kinetics of the Pd nanoparticles along the entire process sequence, revealing significant slowing of the sorption process and apparent activation energy increase in the presence of surfactant molecules on the surface, as well as after plasma treatment when the surfactants have been removed. Only after the thermal annealing step the sorption rates and apparent activation energies are recovered to levels very similar to pristine Pd nanoparticles that had never been exposed to surfactant molecules and plasma treatment. This work thus advertises tailored plasma cleaning and mild heat treatments as effective recipe for the removal of surfactant molecules from nanoparticle surfaces. In a wider perspective, it also highlights the importance of both careful selection of plasma treatment(s) for the cleaning of nanoparticle and extended surfaces and detailed analysis of the impact of the cleaning procedure itself if, for example, the cleaned surfaces are to be used in surface reactions.

## METHODS

**Pd Particle Array Nanofabrication.** Samples were fabricated onto flat surfaces using hole-mask colloidal lithography (HCL) following the procedures detailed elsewhere.<sup>69,70</sup> As substrates we either used fused silica (for the LSPR sensing experiment), a thermally oxidized Si wafer (for XPS and SEM), or in-house fabricated<sup>71</sup> TEM windows (for TEM imaging). In brief, the key steps of the nanofabrication procedure are (i) mask preparation via colloidal PS bead self-assembly, (ii) desired material deposition through the mask, and (iii) mask lift-off. The average diameter of Pd nanodisks targeted here was 190 nm and their thickness was 25 nm. After nanofabrication, the samples were all thermally annealed at 500 °C in 4%  $H_2$  diluted in Ar (total flow 150 mL/min) for 24 h to induce a structurally stable state characterized by a high degree of crystallinity and particles comprising 5–10 crystallites. Notably, their diameter thereby shrinks to about 170 nm, while the thickness increases to ca. 40 nm due to recrystallization.

**Surfactant Coating Procedures.** Three types of surfactants, i.e., CTAB (cetrimonium bromide), CTAC (cetrimonium chloride), and TOAB (tetraoctylammonium bromide) were dissolved in Milli-Q (MQ) water at 10 mM concentration. The solution was then drop cast onto the nanofabricated Pd surfaces and covered with a glass lid for 24 h incubation.<sup>32</sup> Subsequently, the excess surfactant solution was washed away in Milli-Q water and blow-dried with  $N_2$  gas.

**Transmission Electron Microscopy (TEM) and Scanning Electron Microscopy (SEM).** The TEM images were obtained using a Tecnai T20 microscope operating at 200 kV with LaB<sub>6</sub> filament electron gun. The SEM images were acquired using a Zeiss 60 VP operating at 10 kV electron beam energy with working distance of 5 mm.

**Atomic Force Microscopy (AFM).** Measurements were performed using a Dimension 3100 Scanning Probe Microscope from Bruker operated in tapping mode. The height scan was done over an area of  $1 \mu m \times 1 \mu m$  with height resolution 0.1 nm. To process the data (i.e., linescan plot and roughness calculation), the Gwyddion 2.48 software was employed.

**Hydrogen Sorption Kinetics Measurements.** The hydrogen sorption measurements were carried out in a vacuum chamber setup with optical windows reported elsewhere.<sup>72</sup> The absolute hydrogen pressure in the chamber was monitored using two capacitive pressure gauges with different range pressure gauges (MKS Baratron). Optical transmittance through the sample was enabled by UHV-compatible fused silica windows mounted on the vacuum chamber, and by using a fiber-coupled, unpolarized white light source (Avantes AvaLight-Hal) and a fixed grating fiber coupled spectrophotometer (Avantes SensLine AvaSpec-2048XL). The temperature was controlled with a heating coil wrapped around the chamber and a temperature



controller (Eurotherm 3216) in a feedback loop manner, where the sample surface temperature inside the vacuum chamber was continuously used as input. We performed all our experiments at 30 °C. For the activation energy measurements, we measured sorption time traces of the sample at four different temperatures: 60, 50, 40, and 30 °C. The LSPR peak shift were obtained by Lorentzian fitting of the peak and extracting the spectral shift.

**X-ray Photoelectron Spectroscopy (XPS).** A PHI 5000 VersaProbe III (Physical Electronics) was used to confirm surfactant adsorption on the Pd nanoparticles and their removal, as well as to characterize contamination induced by the plasma cleaning process developed. The monochromatized  $K\alpha$  X-rays of Al were used as excitation source. The high-resolution spectra were recorded with an energy step of 0.1 eV and a pass energy of 55 eV. The base pressure was  $<5.0 \times 10^{-7}$  Pa. For surface concentration quantification the Multipak 6.0 software was used. The atomic concentration resolution is in the range of 0.4–1.0 at. %.

**Plasma Cleaning Process.** The plasma cleaning was done in a BatchTop m/95 PlasmaTherm Reactive Ion Etcher (RIE). Each cycle of the  $O_2$  plasma cleaning recipe comprised 60 s exposure to 50 W, 250 mTorr, and 10 sccm and each cycle of the  $H_2$  plasma cleaning recipe comprised 60 s exposure to 100 W, 250 mTorr, and 40 sccm  $H_2$  plasma. For the final recipe, we applied two cycles of sequential  $O_2$  plasma and  $H_2$  plasma (as in  $O_2 \rightarrow H_2 \rightarrow O_2 \rightarrow H_2$ ) to ensure the complete surfactant removal. It is worth noting that order matters:  $O_2$  plasma induces oxidized Pd, and therefore the  $H_2$  plasma is applied after the  $O_2$  plasma to revert the oxidation.

## ■ ASSOCIATED CONTENT

### SI Supporting Information

The Supporting Information is available free of charge at <https://pubs.acs.org/doi/10.1021/acsanm.3c00141>.

XPS quantitative analysis of surfactant removal, hydrogen desorption rate, hydrogen desorption Arrhenius plot and activation energy, XPS analysis of plasma-treatment contamination, TEM images, AFM topography analysis (PDF)

## ■ AUTHOR INFORMATION

### Corresponding Authors

**Christoph Langhammer** – Department of Physics, Chalmers University of Technology, Göteborg 412 96, Sweden; [orcid.org/0000-0003-2180-1379](https://orcid.org/0000-0003-2180-1379); Email: [iwan.darmadi@alumni.ui.ac.id](mailto:iwan.darmadi@alumni.ui.ac.id)

**Iwan Darmadi** – Department of Physics, Chalmers University of Technology, Göteborg 412 96, Sweden; [orcid.org/0000-0002-5921-9336](https://orcid.org/0000-0002-5921-9336); Email: [clangham@chalmers.se](mailto:clangham@chalmers.se)

### Authors

**Jordi Piella** – Department of Physics, Chalmers University of Technology, Göteborg 412 96, Sweden

**Alicja Stolaś** – Department of Chemistry and Chemical Engineering, Chalmers University of Technology, Göteborg 412 96, Sweden; [orcid.org/0000-0002-6736-9553](https://orcid.org/0000-0002-6736-9553)

**Carl Andersson** – Department of Physics, Chalmers University of Technology, Göteborg 412 96, Sweden

**Christopher Tiburski** – Department of Physics, Chalmers University of Technology, Göteborg 412 96, Sweden; [orcid.org/0000-0003-3925-5409](https://orcid.org/0000-0003-3925-5409)

**Kasper Moth-Poulsen** – Department of Chemistry and Chemical Engineering, Chalmers University of Technology, Göteborg 412 96, Sweden; Institute of Materials Science of Barcelona, ICMAB-CSIC, Barcelona ES-08193, Spain; Catalan Institution for Research and Advanced Studies, ICREA, Barcelona ES-08010, Spain; Department of

Chemical Engineering, Universitat Politècnica de Catalunya, EEBE, Barcelona 08019, Spain; [orcid.org/0000-0003-4018-4927](https://orcid.org/0000-0003-4018-4927)

Complete contact information is available at: <https://pubs.acs.org/doi/10.1021/acsanm.3c00141>

## Author Contributions

I.D., A.S., K.M.P., and C.L. designed the experiment. I.D. fabricated the Pd nanodisks. I.D. and C.L. wrote the manuscript. J.P. assisted with the manuscript writing. K.M.P. proof-read the manuscript. J.P. and A.S. prepared the surfactant deposition. I.D. performed the hydrogenation kinetics measurement. I.D. and J.P. performed the TEM imaging and analysis. I.D. performed the AFM measurement and analysis. C.T., C.A., and I.D. performed the XPS measurement and data analysis. C.L. coordinated the project.

## Notes

The authors declare no competing financial interest.

## ■ ACKNOWLEDGMENTS

We acknowledge financial support from the Swedish Foundation for Strategic Research framework project RMA15-0052 (C.L.) and the Knut and Alice Wallenberg Foundation project 2016.0210 (C.L.) and the Wenner-Gren Foundation via contract UPD2020-0287 (J.P.). We thank Dr. Sara Nilsson for fruitful discussion of the TEM images. Part of this work was carried out at the Chalmers MC2 Cleanroom Facility and at the Chalmers Materials Analysis Laboratory (CMAL).

## ■ REFERENCES

- (1) Tiburski, C.; Boje, A.; Nilsson, S.; Say, Z.; Fritzsche, J.; Ström, H.; Hellman, A.; Langhammer, C. Light-Off in Plasmon-Mediated Photocatalysis. *ACS Nano* **2021**, *15* (7), 11535–11542.
- (2) Pekkari, A.; Say, Z.; Susarrey-Arce, A.; Langhammer, C.; Härelind, H.; Sebastian, V.; Moth-Poulsen, K. Continuous Microfluidic Synthesis of Pd Nanocubes and PdPt Core-Shell Nanoparticles and Their Catalysis of NO<sub>2</sub> Reduction. *ACS Appl. Mater. Interfaces* **2019**, *11* (39), 36196–36204.
- (3) Zhang, H.; Jin, M.; Xiong, Y.; Lim, B.; Xia, Y. Shape-Controlled Synthesis of Pd Nanocrystals and Their Catalytic Applications. *Acc. Chem. Res.* **2013**, *46* (8), 1783–1794.
- (4) Schneemann, A.; White, J. L.; Kang, S.; Jeong, S.; Wan, L. F.; Cho, E. S.; Heo, T. W.; Prendergast, D.; Urban, J. J.; Wood, B. C.; et al. Nanostructured Metal Hydrides for Hydrogen Storage. *Chemical Reviews* **2018**, *118*, 10775–10839.
- (5) Yamauchi, M.; Ikeda, R.; Kitagawa, H.; Takata, M. Nanosize Effects on Hydrogen Storage in Palladium. *J. Phys. Chem. C* **2008**, *112* (9), 3294–3299.
- (6) Conde, J. J.; Maroño, M.; Sánchez-Hervás, J. M. Pd-Based Membranes for Hydrogen Separation: Review of Alloying Elements and Their Influence on Membrane Properties. *Sep. Purif. Rev.* **2017**, *46* (2), 152–177.
- (7) Bernardo, G.; Araújo, T.; da Silva Lopes, T.; Sousa, J.; Mendes, A. Recent Advances in Membrane Technologies for Hydrogen Purification. *Int. J. Hydrogen Energy* **2020**, *45* (12), 7313–7338.
- (8) Darmadi, I.; Nugroho, F. A. A.; Langhammer, C. High-Performance Nanostructured Palladium-Based Hydrogen Sensors - Current Limitations and Strategies for Their Mitigation. *ACS Sensors* **2020**, *5*, 3306–3327.
- (9) Wadell, C.; Syrenova, S.; Langhammer, C. Plasmonic Hydrogen Sensing with Nanostructured Metal Hydrides. *ACS Nano* **2014**, *8*, 11925–11940.
- (10) Lerch, S.; Stolaś, A.; Darmadi, I.; Wen, X.; Strach, M.; Langhammer, C.; Moth-Poulsen, K. Robust Colloidal Synthesis of

Palladium-Gold Alloy Nanoparticles for Hydrogen Sensing. *ACS Appl. Mater. Interfaces* **2021**, *13* (38), 45758–45767.

(11) Östergren, I.; Pourrahimi, A. M.; Darmadi, I.; Da Silva, R.; Stolaš, A.; Lerch, S.; Berke, B.; Guizar-Sicairos, M.; Liebi, M.; Foli, G.; Palermo, V.; Minelli, M.; Moth-Poulsen, K.; Langhammer, C.; Müller, C. Highly Permeable Fluorinated Polymer Nanocomposites for Plasmonic Hydrogen Sensing. *ACS Appl. Mater. Interfaces* **2021**, *13* (18), 21724–21732.

(12) Nugroho, F. A. A.; Bai, P.; Darmadi, I.; Castellanos, G. W.; Fritzsche, J.; Langhammer, C.; Gómez Rivas, J.; Baldi, A. Inverse Designed Plasmonic Metasurface with Parts per Billion Optical Hydrogen Detection. *Nat. Commun.* **2022**, *13* (1), 5737.

(13) Züttel, A.; Remhof, A.; Borgschulte, A.; Friedrichs, O. Hydrogen: The Future Energy Carrier. *Philos. Trans. R. Soc. A Math. Phys. Eng. Sci.* **2010**, *368* (1923), 3329–3342.

(14) Dekura, S.; Kobayashi, H.; Kusada, K.; Kitagawa, H. Hydrogen in Palladium and Storage Properties of Related Nanomaterials: Size, Shape, Alloying, and Metal-Organic Framework Coating Effects. *ChemPhysChem* **2019**, *20*, 1158–1176.

(15) *Hydrogen in Intermetallic Compounds II*; Schlapbach, L., Ed.; Topics in Applied Physics; Springer Berlin Heidelberg: Berlin, 1992; Vol. 67.

(16) Dietze, E. M.; Chen, L.; Grönbeck, H. Surface Steps Dominate the Water Formation on Pd(111) Surfaces. *J. Chem. Phys.* **2022**, *156* (6), 064701.

(17) Andersson, M.; Rosén, A. Adsorption and Reactions of O<sub>2</sub> and D<sub>2</sub> on Small Free Palladium Clusters in a Cluster–Molecule Scattering Experiment. *J. Phys.: Condens. Matter* **2010**, *22* (33), 334223.

(18) Koo, W. T.; Qiao, S.; Ogata, A. F.; Jha, G.; Jang, J. S.; Chen, V. T.; Kim, I. D.; Penner, R. M. Accelerating Palladium Nanowire H<sub>2</sub> Sensors Using Engineered Nanofiltration. *ACS Nano* **2017**, *11* (9), 9276–9285.

(19) Slaman, M.; Westerwaal, R.; Schreuders, H.; Dam, B. Optical Hydrogen Sensors Based on Metal-Hydrides. In *Photonic Applications for Aerospace, Transportation, and Harsh Environment III*; Kazemi, A. A., Javahiraly, N., Panahi, A. S., Thibault, S., Kress, B. C., Eds.; International Society for Optics and Photonics, 2012; Vol. 8368, pp 836805–836808.

(20) Nugroho, F. A. A.; Darmadi, I.; Cusinato, L.; Susarrey-Arce, A.; Schreuders, H.; Bannenberg, L. J.; da Silva Fanta, A. B.; Kadkhodazadeh, S.; Wagner, J. B.; Antosiewicz, T. J.; et al. Metal–Polymer Hybrid Nanomaterials for Plasmonic Ultrafast Hydrogen Detection. *Nat. Mater.* **2019**, *18* (5), 489–495.

(21) Adams, B. D.; Chen, A. The Role of Palladium in a Hydrogen Economy. *Mater. Today* **2011**, *14*, 282–289.

(22) Behm, R. J.; Penka, V.; Cattania, M.-G.; Christmann, K.; Ertl, G. Evidence for “Subsurface” Hydrogen on Pd(110): An Intermediate between Chemisorbed and Dissolved Species. *J. Chem. Phys.* **1983**, *78* (12), 7486–7490.

(23) Johnson, N. J. J.; Lam, B.; MacLeod, B. P.; Sherbo, R. S.; Moreno-Gonzalez, M.; Fork, D. K.; Berlinguette, C. P. Facets and Vertices Regulate Hydrogen Uptake and Release in Palladium Nanocrystals. *Nat. Mater.* **2019**, *18*, 454–458.

(24) Darmadi, I.; Khairunnisa, S. Z.; Tomeček, D.; Langhammer, C. Optimization of the Composition of PdAuCu Ternary Alloy Nanoparticles for Plasmonic Hydrogen Sensing. *ACS Appl. Nano Mater.* **2021**, *4* (9), 8716–8722.

(25) Darmadi, I.; Nugroho, F. A. A.; Kadkhodazadeh, S.; Wagner, J. B.; Langhammer, C. Rationally Designed PdAuCu Ternary Alloy Nanoparticles for Intrinsically Deactivation-Resistant Ultrafast Plasmonic Hydrogen Sensing. *ACS Sensors* **2019**, *4* (5), 1424–1432.

(26) Darmadi, I.; Stolaš, A.; Östergren, I.; Berke, B.; Nugroho, F. A. A.; Minelli, M.; Lerch, S.; Tanyeli, I.; Lund, A.; Andersson, O.; Zhdanov, V. P.; Liebi, M.; Moth-Poulsen, K.; Müller, C.; Langhammer, C. Bulk-Processed Pd Nanocube–Poly(Methyl Methacrylate) Nanocomposites as Plasmonic Plastics for Hydrogen Sensing. *ACS Appl. Nano Mater.* **2020**, *3* (8), 8438–8445.

(27) Kamakoti, P.; Morreale, B. D.; Ciocco, M. V.; Howard, B. H.; Killmeyer, R. P.; Cugini, A. V.; Sholl, D. S. Prediction of Hydrogen Flux Through Sulfur-Tolerant Binary Alloy Membranes. *Science* (80-.) **2005**, *307* (5709), 569–573.

(28) Morreale, B. D.; Ciocco, M. V.; Howard, B. H.; Killmeyer, R. P.; Cugini, A. V.; Enick, R. M. Effect of Hydrogen-Sulfide on the Hydrogen Permeance of Palladium-Copper Alloys at Elevated Temperatures. *J. Membr. Sci.* **2004**, *241* (2), 219–224.

(29) Say, Z.; Kaya, M.; Kaderoglu, Ç.; Koçak, Y.; Ercan, K. E.; Sika-Nartey, A. T.; Jalal, A.; Turk, A. A.; Langhammer, C.; Jahangirzadeh Varjovi, M.; et al. Unraveling Molecular Fingerprints of Catalytic Sulfur Poisoning at the Nanometer Scale with Near-Field Infrared Spectroscopy. *J. Am. Chem. Soc.* **2022**, *144*, 8848.

(30) Cookson, J. The Preparation of Palladium Nanoparticles. *Platin. Met. Rev.* **2012**, *56* (2), 83–98.

(31) Li, C.; Sato, T.; Yamauchi, Y. Size-Controlled Synthesis of Mesoporous Palladium Nanoparticles as Highly Active and Stable Electrocatalysts. *Chem. Commun.* **2014**, *50* (79), 11753–11756.

(32) Stolaš, A.; Darmadi, I.; Nugroho, F. A. A.; Moth-Poulsen, K.; Langhammer, C. Impact of Surfactants and Stabilizers on Palladium Nanoparticle–Hydrogen Interaction Kinetics: Implications for Hydrogen Sensors. *ACS Appl. Nano Mater.* **2020**, *3* (3), 2647–2653.

(33) Johnson, N. J. J.; Lam, B.; Sherbo, R. S.; Fork, D. K.; Berlinguette, C. P. Ligands Affect Hydrogen Absorption and Desorption by Palladium Nanoparticles. *Chem. Mater.* **2019**, *31* (21), 8679–8684.

(34) Heuer-Jungemann, A.; Feliu, N.; Bakaimi, I.; Hamaly, M.; Alkilany, A.; Chakraborty, I.; Masood, A.; Casula, M. F.; Kostopoulou, A.; Oh, E.; et al. The Role of Ligands in the Chemical Synthesis and Applications of Inorganic Nanoparticles. *Chemical Reviews* **2019**, *119*, 4819–4880.

(35) Nikoobakht, B.; El-Sayed, M. A. Evidence for Bilayer Assembly of Cationic Surfactants on the Surface of Gold Nanorods. *Langmuir* **2001**, *17* (20), 6368–6374.

(36) Sui, Z. M.; Chen, X.; Wang, L. Y.; Xu, L. M.; Zhuang, W. C.; Chai, Y. C.; Yang, C. J. Capping Effect of CTAB on Positively Charged Ag Nanoparticles. *Phys. E Low-Dimensional Syst. Nanostructures* **2006**, *33* (2), 308–314.

(37) Cookson, J. The Preparation of Palladium Nanoparticles. *Platin. Met. Rev.* **2012**, *56* (2), 83–98.

(38) Gómez-Graña, S.; Hubert, F.; Testard, F.; Guerrero-Martínez, A.; Grillo, I.; Liz-Marzán, L. M.; Spalla, O. Surfactant (Bi)Layers on Gold Nanorods. *Langmuir* **2012**, *28* (2), 1453–1459.

(39) Lohse, S. E.; Burrows, N. D.; Scarabelli, L.; Liz-Marzán, L. M.; Murphy, C. J. Anisotropic Noble Metal Nanocrystal Growth: The Role of Halides. *Chem. Mater.* **2014**, *26* (1), 34–43.

(40) Niu, W.; Zhang, L.; Xu, G. Shape-Controlled Synthesis of Single-Crystalline Palladium Nanocrystals. *ACS Nano* **2010**, *4* (4), 1987–1996.

(41) Lohse, S. E.; Murphy, C. J. The Quest for Shape Control: A History of Gold Nanorod Synthesis. *Chem. Mater.* **2013**, *25* (8), 1250–1261.

(42) Meena, S. K.; Celiksoy, S.; Schäfer, P.; Henkel, A.; Sönnichsen, C.; Sulpizi, M. The Role of Halide Ions in the Anisotropic Growth of Gold Nanoparticles: A Microscopic, Atomistic Perspective. *Phys. Chem. Chem. Phys.* **2016**, *18* (19), 13246–13254.

(43) Pu, H.; Dai, H.; Zhang, T.; Dong, K.; Wang, Y.; Deng, Y. Metal Nanoparticles with Clean Surface: The Importance and Progress. *Current Opinion in Electrochemistry* **2022**, *32*, 100927.

(44) Lu, L.; Lou, B.; Zou, S.; Kobayashi, H.; Liu, J.; Xiao, L.; Fan, J. Robust Removal of Ligands from Noble Metal Nanoparticles by Electrochemical Strategies. *ACS Catal.* **2018**, *8* (9), 8484–8492.

(45) Nareish, N.; Wasim, F. G. S.; Ladewig, B. P.; Neergat, M. Removal of Surfactant and Capping Agent from Pd Nanocubes (Pd-NCs) Using Tert-Butylamine: Its Effect on Electrochemical Characteristics. *J. Mater. Chem. A* **2013**, *1* (30), 8553–8559.

(46) Crespo-Quesada, M.; Andanson, J.-M.; Yarulin, A.; Lim, B.; Xia, Y.; Kiwi-Minsker, L. UV–Ozone Cleaning of Supported Poly(Vinylpyrrolidone)-Stabilized Palladium Nanocubes: Effect of Stabil-

izer Removal on Morphology and Catalytic Behavior. *Langmuir* **2011**, *27* (12), 7909–7916.

(47) Nojiri, K. Mechanism of Dry Etching. In *Dry Etching Technology for Semiconductors*; Springer International Publishing, 2015; pp 11–30.

(48) Fredriksson, H.; Alaverdyan, Y.; Dmitriev, A.; Langhammer, C.; Sutherland, D. S.; Zäch, M.; Kasemo, B. Hole-Mask Colloidal Lithography. *Adv. Mater.* **2007**, *19* (23), 4297–4302.

(49) Nugroho, F. A. A.; Darmadi, I.; Zhdanov, V. P.; Langhammer, C. Universal Scaling and Design Rules of Hydrogen-Induced Optical Properties in Pd and Pd-Alloy Nanoparticles. *ACS Nano* **2018**, *12* (10), 9903–9912.

(50) Alekseeva, S.; Fanta, A. B. da S.; Iandolo, B.; Antosiewicz, T. J.; Nugroho, F. A. A.; Wagner, J. B.; Burrows, A.; Zhdanov, V. P.; Langhammer, C. Grain Boundary Mediated Hydriding Phase Transformations in Individual Polycrystalline Metal Nanoparticles. *Nat. Commun.* **2017**, *8* (1), 1084.

(51) Delmelle, R.; Amin-Ahmadi, B.; Sinnaeve, M.; Idrissi, H.; Pardoën, T.; Schryvers, D.; Proost, J. Effect of Structural Defects on the Hydriding Kinetics of Nanocrystalline Pd Thin Films. *Int. J. Hydrogen Energy* **2015**, *40* (23), 7335–7347.

(52) Borodko, Y.; Jones, L.; Lee, H.; Frei, H.; Somorjai, G. Spectroscopic Study of Tetradecyltrimethylammonium Bromide Pt-C14TAB Nanoparticles: Structure and Stability. *Langmuir* **2009**, *25* (12), 6665–6671.

(53) de Barros, H. R.; Piovan, L.; Sasaki, G. L.; de Araujo Sabry, D.; Mattoso, N.; Nunes, A. M.; Meneghetti, M. R.; Riegel-Vidotti, I. C. Surface Interactions of Gold Nanorods and Polysaccharides: From Clusters to Individual Nanoparticles. *Carbohydr. Polym.* **2016**, *152*, 479–486.

(54) Heinz, H.; Pramanik, C.; Heinz, O.; Ding, Y.; Mishra, R. K.; Marchon, D.; Flatt, R. J.; Estrela-Lopis, I.; Llop, J.; Moya, S.; Ziolo, R. F. Nanoparticle Decoration with Surfactants: Molecular Interactions, Assembly, and Applications. *Surf. Sci. Rep.* **2017**, *72* (1), 1–58.

(55) Heinz, H.; Vaia, R. A.; Farmer, B. L. Relation between Packing Density and Thermal Transitions of Alkyl Chains on Layered Silicate and Metal Surfaces. *Langmuir* **2008**, *24* (8), 3727–3733.

(56) Langhammer, C.; Zhdanov, V. P.; Zorić, I.; Kasemo, B. Size-Dependent Kinetics of Hydriding and Dehydriding of Pd Nanoparticles. *Phys. Rev. Lett.* **2010**, *104* (13), 135502.

(57) Amandusson, H.; Ekedahl, L. G.; Dannetun, H. Effect of CO and O<sub>2</sub> on Hydrogen Permeation through a Palladium Membrane. *Appl. Surf. Sci.* **2000**, *153* (4), 259–267.

(58) Li, G.; Kobayashi, H.; Dekura, S.; Ikeda, R.; Kubota, Y.; Kato, K.; Takata, M.; Yamamoto, T.; Matsumura, S.; Kitagawa, H. Shape-Dependent Hydrogen-Storage Properties in Pd Nanocrystals: Which Does Hydrogen Prefer, Octahedron (111) or Cube (100)? *J. Am. Chem. Soc.* **2014**, *136* (29), 10222–10225.

(59) Sytwu, K.; Hayee, F.; Narayan, T. C.; Koh, A. L.; Sinclair, R.; Dionne, J. A. Visualizing Facet-Dependent Hydrogenation Dynamics in Individual Palladium Nanoparticles. *Nano Lett.* **2018**, *18* (9), 5357–5363.

(60) Weber, M. J.; MacKus, A. J. M.; Verheijen, M. A.; Longo, V.; Bol, A. A.; Kessels, W. M. M. Atomic Layer Deposition of High-Purity Palladium Films from Pd(HfAc)<sub>2</sub> and H<sub>2</sub> and O<sub>2</sub> Plasmas. *J. Phys. Chem. C* **2014**, *118* (16), 8702–8711.

(61) Nordlund, K.; Björkas, C.; Ahlgren, T.; Lasa, A.; Sand, A. E. Multiscale Modelling of Plasma-Wall Interactions in Fusion Reactor Conditions. *J. Phys. D: Appl. Phys.* **2014**, *47* (22), 224018.

(62) Sun, C.; Müller, E.; Meffert, M.; Gerthsen, D. Analysis of Crystal Defects by Scanning Transmission Electron Microscopy (STEM) in a Modern Scanning Electron Microscope. *Adv. Struct. Chem. Imaging* **2019**, *5* (1), 1.

(63) Koprucki, T.; Maltzi, A.; Mielke, A. Symmetries in Transmission Electron Microscopy Imaging of Crystals with Strain. *Proc. R. Soc. A Math. Phys. Eng. Sci.* **2022**, *478* (2267), DOI: 10.1098/rspa.2022.0317

(64) Radjabov, T. D.; Alimova, L. Y.; Sharudo, A. V. Low Voltage Hydrogen Plasma Interaction with Palladium Surface. *J. Nucl. Mater.* **1984**, *125* (3), 326–329.

(65) Tsai, C.-H.; Chen, K.-J.; Pan, F.-M.; Lo, H.-Y.; Li, Y.; Chiang, M.-C.; Mo, C.-N. Effects of Hydrogen Plasma Treatment on Field-Emission Characteristics of Palladium Nanogap Emitters. *J. Electrochem. Soc.* **2008**, *155* (12), J361.

(66) Jewell, L. L.; Davis, B. H. Review of Absorption and Adsorption in the Hydrogen-Palladium System. *Applied Catalysis A: General* **2006**, *310*, 1–15.

(67) Johansson, M.; Skúlason, E.; Nielsen, G.; Murphy, S.; Nielsen, R. M.; Chorkendorff, I. Hydrogen Adsorption on Palladium and Palladium Hydride at 1 bar. *Surf. Sci.* **2010**, *604* (7–8), 718–729.

(68) McAlister, A. J. The Al-Pd (Aluminum-Palladium) System. *Bull. Alloy Phase Diagrams* **1986**, *7* (4), 368–374.

(69) Nugroho, F. A. A.; Iandolo, B.; Wagner, J. B.; Langhammer, C. Bottom-Up Nanofabrication of Supported Noble Metal Alloy Nanoparticle Arrays for Plasmonics. *ACS Nano* **2016**, *10* (2), 2871–2879.

(70) Wadell, C.; Nugroho, F. A. A.; Lidström, E.; Iandolo, B.; Wagner, J. B.; Langhammer, C. Hysteresis-Free Nanoplasmonic Pd-Au Alloy Hydrogen Sensors. *Nano Lett.* **2015**, *15* (5), 3563–3570.

(71) Grant, A. W.; Hu, Q. H.; Kasemo, B. Transmission Electron Microscopy “windows” for Nanofabricated Structures. *Nanotechnology* **2004**, *15* (9), 1175–1181.

(72) Darmadi, I. *Polymer-Nanoparticle Hybrid Materials for Plasmonic Hydrogen Detection*; Chalmers University of Technology: Gothenburg, Sweden, 2021.

## Recommended by ACS

### Robust Rules for Optimal Colorimetric Sensing Based on Gold Nanoparticle Aggregation

José Luis Montaña-Priede, Javier Aizpuru, *et al.*

APRIL 13, 2023  
ACS SENSORS

READ 

### Optical Quantification of Metal Ions Using Plasmonic Nanostructured Microbeads Coated with Metal–Organic Frameworks and Ion-Selective Dyes

Tolga Zorlu, Ramon A. Alvarez-Puebla, *et al.*

MARCH 06, 2023  
ACS NANOSCIENCE AU

READ 

### Plasmonic Array at the Liquid–Liquid Interface: A Dual-Mode Optical Sensing Platform for Multianalytes

Minggang Zhao, Ye Ma, *et al.*

DECEMBER 22, 2022  
ANALYTICAL CHEMISTRY

READ 

### Strong $\pi$ -Metal Interaction Enables Liquid Interfacial Nanoarray–Molecule Co-assembly for Raman Sensing of Ultrathin Fentanyl Doped in Heroin, Ketamine, Morphine...

Zhongxiang Ding, Honglin Liu, *et al.*

FEBRUARY 21, 2023  
ACS APPLIED MATERIALS & INTERFACES

READ 

Get More Suggestions >